# A criterion for predicting delamination growth in composite laminates

Huo, L.; Kassapoglou, C.; Alderliesten, R.C.

**DOI**
10.1016/j.matdes.2022.111160

**Publication date**
2022

**Document Version**
Final published version

**Published in**
Materials & Design

Materials & Design 223 (2022) 111160

Contents lists available at ScienceDirect

Materials & Design

journal homepage: www.elsevier.com/locate/matdes

# A criterion for predicting delamination growth in composite laminates

L. Huo *, C. Kassapoglou, R.C. Alderliesten

*Faculty of Aerospace Engineering, Delft University of Technology, P.O. Box 5058, 2600 GB Delft, the Netherlands*

## HIGHLIGHTS

- A physically sound Hashin-type delamination-propagation criterion containing only a single stress component and single strength parameter is developed.
- The fibre direction delamination growth of multidirectional carbon fibre-reinforced polymer laminates can be precisely predicted by using the proposed criterion.
- The specific stress component that drives the fibre direction delamination growth is $\sigma_{13}$, and the growth threshold is $S_{13}$.
- At the microscopic level, the fibre direction delamination fronts can be either opening crack-dominated or sliding crack-dominated.

## GRAPHICAL ABSTRACT

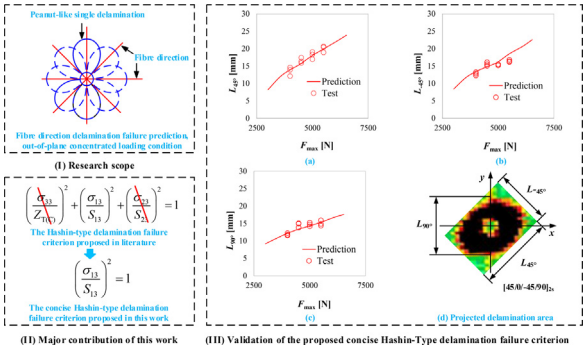


## ARTICLE INFO

*Article history:*
Received 14 June 2022
Revised 12 September 2022
Accepted 13 September 2022
Available online 14 September 2022

*Keywords:*
Polymer-matrix composites
Quasi-static indentation
Delamination failure prediction
Finite element analysis

## ABSTRACT

To develop a simplified and physically sound delamination-failure criterion, this paper reports a joint experimental and numerical study in which out-of-plane quasi-static indentations with different indentation forces were applied to the centre of fully clamped rectangular carbon fibre-reinforced polymer (CFRP) laminates. The results show that two basic micro-delamination growth modes, which are separately dominated by opening and sliding microcracks, can be distinguished according to the fracture morphologies of the delaminations along the 0° fibre direction. Both are driven by the out-of-plane shear stress $\sigma_{13}$, and the corresponding delamination failure threshold is the out-of-plane shear strength $S_{13}$. Based on these results, a concise Hashin-type delamination-propagation criterion containing only a single stress component and single strength parameter is proposed, which, by incorporating it into the finite element model, the delamination growth along the fibre directions of multidirectional CFRP laminates can be precisely predicted; the prediction error is less than 10 %.


## 1. Introduction

Owing to their high strength-to-mass and stiffness-to-mass ratios, carbon fibre-reinforced polymer (CFRP) composites are considered ideal materials for lightweight applications. The wing and fuselage skin of some modern aircraft, such as Boeing 787 [1] and Airbus A350 XWB [2], are fabricated from laminated CFRP composites. However, the major obstacle to the application of CFRP composites is their susceptibility to out-of-plane loading (i.e. impacts and quasi-static indentations) because of their low out-of-plane strengths [3]. Many studies have focused on the damages that occur in CFRP composite structures under such loading [4–9], especially those caused by low-velocity impact, which is generally difficult to detect during routine maintenance [10–12].

* Corresponding author.
*E-mail address:* L.Huo@tudelft.nl (L. Huo).

https://doi.org/10.1016/j.matdes.2022.111160
0264-1275/

The modelling of the damage of composite laminates under various loading conditions, including out-of-plane impact and indentation cases, is a popular topic and has attracted the interest of many researchers over the past few decades [13–16]. Generally, damages in composite materials are in the form of matrix cracking, fibre failure, and delamination, and numerous damage criteria have been proposed in the literature to predict these three basic damage modes. Based on different assumptions, these damage criteria can be divided into stress-based and fracture-mechanics-based criteria [17]. The stress-based damage criteria assume that both damage initiation and propagation are due to the stress states satisfying certain critical conditions, whereas the fracture-mechanics-based criteria assume that any damage results from the growth of inherent material defects.

A review of methodologies for modelling composite material structural and damage behaviours by Orifici et al. [18] showed that the most accepted criteria for predicting fibre and matrix failures in tension/compression are stress-based. However, for the prediction of delamination initiation and propagation, different types of failure criteria are employed [19–22]: a stress-based failure criterion is used to predict the initiation, and a fracture-mechanics-based criterion is used for the subsequent propagation. The major considerations for adopting such a modelling strategy, which considers composite laminates under out-of-plane impact loading as an example, are as follows:

Extensive studies have shown that delamination in impacted composite laminates is induced by matrix cracks rather than by the growth of inherent material defects [4,11,23]. The fracture-mechanics-based methods to predict delamination propagation cannot automatically locate these matrix cracks, and arbitrarily specifying the points at which the delaminations begin to propagate is unreasonable.

Stress concentrations can result in misleading predictions when stress-based criteria are adopted to address delamination-propagation problems. Inherent defects, such as voids, microcracking, delamination, and wrinkles, are considered to be the major stress raisers in composite laminates. Moreover, these inherent defects may significantly influence delamination growth in impacted/indented composite laminates, which makes fracture mechanics methods more suitable for predicting delamination growth.

Although fracture-mechanics-based criteria are superior to stress-based criteria in addressing delamination growth problems, the problem is that, as shown in Table 1, most of the fracture-mechanics-based delamination growth criteria involve exponents or other non-energy parameters obtained from curve fitting. This may raise concerns that the curve fit parameters used to characterise delamination growth are not physically sound, which may obscure the actual delamination growth mechanisms and the associated delamination growth-driven forces. In contrast, as shown in Table 2, most of the stress-based delamination failure criteria proposed in the literature are used to predict delamination failures without such curve fit parameters. More importantly, the expressions of these criteria can provide a good understanding of the underlying causes of delamination propagation. However, a common problem in the development of these two branches of delamination criteria is that they tend to be overly complex. A concise, valid, effective, efficient, and physically sound delamination growth criterion is necessary and crucial for delamination growth prediction.However, several steps are necessary before this delamination failure criterion can be fully optimised. As a first step toward this, this study aimed to develop a simplistic but robust stress-based delamination criterion for predicting delamination failure in composite laminates subjected to out-of-plane indentation loading. Hence, it is necessary to further investigate and quantify the effect of in-plane and out-of-plane stresses on delamination growth; therefore, an experimental and numerical study was undertaken. Quasi-static indentations with different indentation forces were applied to the centre of the clamped composite laminates to introduce different damage levels. Ultrasonic C-scanning and optical microscopy were used to establish the damage state post-mortem. Finite element (FE) analysis using ABAQUS, which considered various damages and material mechanical degradations, was used to determine the stress states of the experimentally observed delamination fronts.

**Table 1**
Fracture-mechanics-based delamination growth criteria [18].

| Expression | Parameter obtained from curve fitting | Reference |
|---|---|---|
| $G_t = G_{IIc} - (G_{IIc} - G_{Ic})\sqrt{\frac{G_I}{G_{Ic}}}$ | – | Hahn [24] |
| $G_t = (G_{Ic} - \chi) + \chi\sqrt{1 + \frac{G_{II}}{G_I}\sqrt{\frac{E_{11}}{E_{22}}}}$ | $\chi$ | Hahn and Johnnesson [25] |
| $\left(\frac{G_I}{G_{Ic}}\right)^m + \left(\frac{G_{II}}{G_{IIc}}\right)^n + \left(\frac{G_{II}}{G_{IIc}}\right)^h = 1$ | m, n, h | Whitcomb [26] |
| $G_t = (G_{Ic} - G_{IIc}) + e^{\gamma\left(1-\sqrt{1+\frac{G_{II}}{G_I}\sqrt{\frac{E_{11}}{E_{22}}}}\right)}$ | $\gamma$ | Donaldson [27] |
| Mode I:$G_I = 3G_{Ic}\sqrt{\frac{E_{22}}{E_{11}}}\left[\frac{G_{Ic}}{G_{II}}\left(\frac{G_{IIc}}{G_{Ic}}\right)^2 - \frac{G_{II}}{G_{Ic}}\right]$<br>Mode II:$G_{II} = \frac{1}{3}G_{IIc}\sqrt{\frac{E_{11}}{E_{22}}}\left(\frac{G_{Ic}}{G_I} - \frac{G_I}{G_{Ic}}\right)$ | – | Hashemi and Kinloch [28] |
| $G_t = (G_{IIc} - G_{Ic}) + e^{\eta\sqrt{\frac{G_I}{G_{II}}}}$ | $\eta$ | White [29] |
| $\frac{G_I}{G_{Ic}} + (\kappa - 1)\frac{G_I G_{II}}{G_{Ic} G_{IIc}} + \frac{G_{II}}{G_{IIc}} = 1$ | $\kappa$ | Hashemi and Kinloch [30] |
| $G_t = G_{Ic} - \rho\frac{G_{II}}{G_I} + \tau\left(\frac{G_{II}}{G_I}\right)^2$ | $\rho$, $\tau$ | Yan et al. [31] |
| $\frac{G_I}{G_{Ic}} + \left(\frac{\kappa-1+\varphi}{1+\frac{G_{II}}{G_I}}\right)\frac{G_I G_{II}}{G_{Ic} G_{IIc}} + \frac{G_{II}}{G_{IIc}} = 1$ | $\kappa$, $\varphi$ | Hashemi and Williams [32] |
| $G_t = G_{Ic} + (G_{IIc} - G_{Ic})\left[\frac{G_{II}}{(G_I + G_{II})}\right]^\eta$ | $\eta$ | Benzeggagh and Kenane [33] |

Note: $G_i$ (i = I, II, and III) are the strain energy release rates related to Mode I, II, and III cracks, and $G_{iC}$ are the corresponding critical strain energy release rates, $G_t$ is the sum of $G_i$, $E_{11}$ and $E_{22}$ are the Young's moduli, and e is the Euler's number.

## 2. Details of the finite element (FE) model and test method

### 2.1. FE model

To achieve the proposed research object, the indentation stress field has to be correctly determined; in particular, the stress states at the delamination fronts must be fully understood. However, it is impossible to directly measure the stress fields in experiments with current stress measurement techniques. The stress field obtained through analytical methods may be misleading owing to the excessive assumptions and simplifications that must be adopted. Alternatively, a calibrated FE model can be used to directly determine indentation stress fields. An overview of the adopted methodology for determining the stress states at the delamination fronts is provided below:

- Obtain the coordinates of the delamination fronts which are observed experimentally;
- Measure the stress states numerically by calculating the stresses at the point in the FE model with the same coordinate as the delamination front.

In this study, an M30SC/DT120 carbon/epoxy composite panel with a quasi-isotropic layup sequence $[45/0/-45/90]_{2s}$ and a geometry size of 150 mm × 300 mm × 2.5 mm under a fully clamped boundary condition was used for the FE modelling. To improve

**Table 2**
Stress-based delamination failure criteria.

| Expression | References |
|---|---|
| $\left(\frac{\sigma_{33}}{Z_T}\right)^2+\left(\frac{\sigma_{13}}{S_{13}}\right)^2+\left(\frac{\sigma_{23}}{S_{23}}\right)^2=1$ *or* $\left(\frac{\sigma_{33}}{Z_C}\right)^2+\left(\frac{\sigma_{13}}{S_{13}}\right)^2+\left(\frac{\sigma_{23}}{S_{23}}\right)^2=1$ | Tserpes et al. [34] |
| $\frac{\sigma_{33}}{Z_T}=1$ *or* $\frac{\sqrt{(\sigma_{12}^2+\sigma_{13}^2)}}{S_{13}}=1$ | Lee [35] |
| $\left(\frac{\sigma_{33}}{Z_T}\right)^2+\frac{\sigma_{13}^2+\sigma_{23}^2}{S_{23}^2}=1$ | Ochoa and Engblom [36] |
| $\left(\frac{\sigma_{33}}{Z_C}\right)^2+\left(\frac{\sigma_{23}}{S_{23}}\right)^2=1$ | Long [37] |
| $\left(\frac{\sigma_{33}}{Z_T}\right)^2+\left(\frac{\sigma_{13}}{S_\tau}\right)^2+\left(\frac{\sigma_{23}}{S_\tau}\right)^2=1$ | Luo and Green [38] |
| $\frac{\sigma_{33}}{Z_T}=1$ *and* $\frac{\sqrt{(\sigma_{12}^2+\sigma_{13}^2)}}{S_{13}}=1$ | Zhang [39] |
| $\left(\frac{\lvert\sigma_{11}^*\rvert}{Y_{T,C}}\right)+\left(\frac{\sigma_{11}^*}{Y_{T,C}}\right)^2+\left(\frac{\lvert\sigma_{22}^*\rvert}{Y_{T,C}}\right)+\left(\frac{\sigma_{22}^*}{Y_{T,C}}\right)^2+\left(\frac{2\lvert\sigma_{11}^*\sigma_{22}^*\rvert}{Y_{T,C}^2}\right)+\left(\frac{\lvert\sigma_{13}\rvert_n}{S_\tau}\right)+\left(\frac{\sigma_{13n}}{S_\tau}\right)^2=1,\ \left(\sigma_{11}^*,\sigma_{22}^*=\frac{\sigma_{11}+\sigma_{22}}{2}\pm\sqrt{\left(\frac{\sigma_{11}-\sigma_{22}}{2}\right)^2+\sigma_{13}^2}\right)$ | De Moura and Marques [40] |

Note: the 1-direction is parallel to the fibre direction, 2-direction is normal to the fibre direction, and 3-direction is parallel to the out-of-plane direction, $S_{ij}$ (i = 1, 2, 3; j = 1, 2, 3, i ≠ j), $S_\tau$ are the shear strength parameters, Y and Z are the strengths normal to the fibre direction with Z out-of-plane, C and T are separately referred to as compressive and tensile.

the computational accuracy, geometric nonlinearity was considered, and the contact area was meshed with a higher mesh density than that of other regions. The steel hemispherical indenter with a diameter of 25 mm was modelled as a discrete rigid body and meshed with four-node 3D bilinear rigid quadrilateral (R3D4) elements.

To simulate the four-side clamped boundary condition, as shown in Fig. 1(a), all degrees of freedom (DOF) in the regions close to the plate edges are constrained, which are marked as 'Fixed'. In this simulation, the load was applied to the geometric centre of the plate. To obtain the force–deflection curve, the displacement at the interface of the indenter with the laminates was used to approximate the deflection of the plate, and the contact force was calculated using a built-in algorithm in ABAQUS.

Moreover, the contact between the indenter and plate's surface was set as a surface-to-surface type, for which the normal behaviour was considered 'Hard' and the tangential behaviour was described through the penalty method with a friction coefficient of 0.3 [41]. A sensitivity study, which changed the friction coefficient from 0.2 to 0.4, was conducted, and only negligible variations were observed in the corresponding force deflection curves. To accurately determine the in-plane and out-of-plane stresses by this FE model, layers of the composite laminate were meshed with the solid element C3D8I (8-node linear brick, incompatible models), with a thickness of 0.15 mm, which was equal to the ply thickness.

More importantly, this FE model was applied with a published ABAQUS user-defined material subroutine, UMAT [42], to account for material stiffness degradation owing to matrix cracks and fibre failures. The puck failure criterion [43] and the constant-stress-exposure gradual-stiffness-degradation method were coded in this UMAT. The relevant elastic material properties which can be found in [44] and strength parameters for the FE model are summarised in Tables 3 and 4, respectively. The strength parameters were provided by the manufacturer. Delamination was not directly modelled in this study; although it may degrade the bending stiffness [45], it is a contributor to stress concentration, and thus significantly alters the local stress field. However, it is generally confined to and/or around the contact area for an intended composite laminate and is considered to have negligible effects on the distribution of the global indentation stress field. The global indentation stress distribution was more important for the results of this research than the local distribution. The reasonableness of such model simplification was provided in the validation and verification of the FE model (Section 3).

## 3. Test method

5. Material and test fixture.

For consistency with the FE model, the CFRP panels were created from unidirectional carbon/epoxy prepreg M30SC/DT120 supplied by Delta-Tech S.p.a. using hand layup, with a stacking sequence of $[45/0/-45/90]_{2s}$. After the hand layup, the laminates were placed in an autoclave at a pressure of 6 bar and cured at 120 ℃ for 90 min. Subsequently, the panels were cut into small specimens with the same dimensions as the FE model shown in Fig. 1(a) using a diamond saw. Before testing, all the specimens were ultrasonically C-scanned, and the specimens without defects were used for the tests to avoid the negative influence of inherent damage on the test results.

In addition, the test fixtures recommended by ASTM standards D6264/D6264M-17 [46] and D7136/D7136M-20 [47] could not supply-four-side clamped boundary conditions similar to the FE model; thus, a new fixture was designed (Fig. 1(b)). With this test fixture, the short edges of the plate were fixed with bolts, whereas the long edges were fixed through clamping pressure.

### 3.1. Test details

Quasi-static indentation tests were conducted using a Zwick Roell 20 kN servo-hydraulic universal material test machine (Fig. 1(c)). The indentation loads were applied to the centre of the specimens using a hemispherical indenter with a diameter of 25 mm and a loading rate of 15 mm/min. The signals of the contact forces and deflections of the plates were recorded using a force and displacement transducer mounted on the top of the indenter fixing device. In addition, the loading and unloading phases of the indentation tests were both displacement controlled. The unloading phase began when the maximum indentation force ($F_{max}$) was reached during the loading process. The $F_{max}$ values for the different specimens were 1500, 2500, 3000, 4000, 4500, 5000, and 5500 N, respectively. The test details are listed in Table 5.

### 3.2. Damage detection

After the indentation test, ultrasonic C-scanning was performed to obtain the projected damage areas. Then, one specimen in each group shown in Table 5 was sectioned along the red line shown in Fig. 1(d), and three specimens from group QSI_07 were sectioned along the blue line. Subsequently, the exposed cross-sectional surfaces were ground with sandpaper with different grain sizes of they were 82, 46.2, 18, 8 and 5 μm, respectively, and were polished using diamond pastes. Finally, the prepared samples were observed under a KEYENCE laser microscope at 5 × and 50 × magnifications., The acquired damage images were processed using AutoCAD 2021 software to facilitate subsequent fracture analysis.

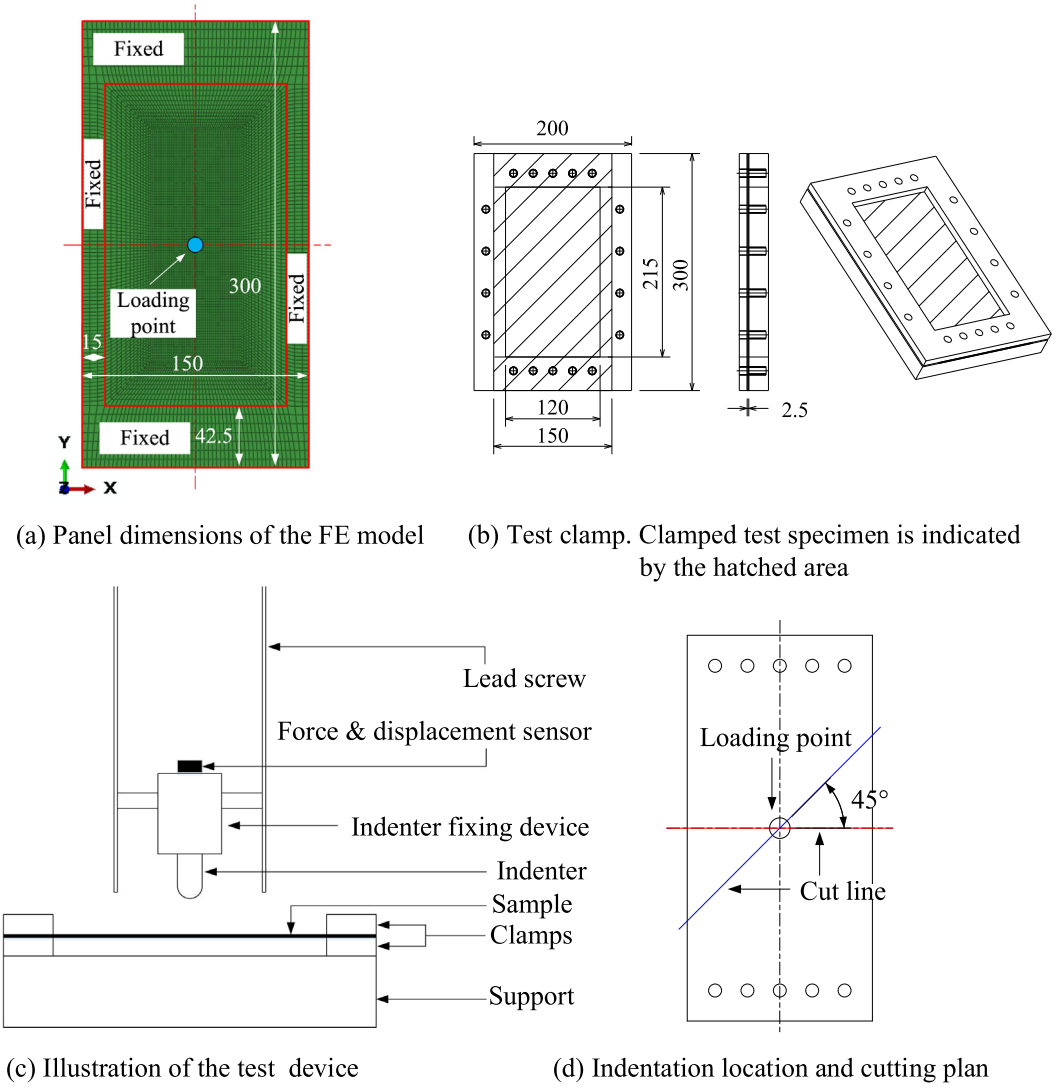


(a) Panel dimensions of the FE model

(b) Test clamp. Clamped test specimen is indicated by the hatched area

(c) Illustration of the test device

(d) Indentation location and cutting plan

**Fig. 1.** Details of the FE model dimensions and quasi-static indentation test.

**Table 3**
Elastic material properties for M30SC/DT120 unidirectional composite laminate [44].

| | |
|---|---|
| Density | $\rho$ = 1.76 g/cm$^3$ |
| Young's modulus of material | $E_{11}$ = 155 GPa, $E_{22} = E_{33}$ = 7.8 GPa, $G_{12} = G_{13}$ = 5.5 GPa, $G_{23}$ = 3.25 GPa* |
| Poisson's ratio | $\nu_{12} = \nu_{13}$ = 0.27, $\nu_{23}$ = 0.2* |

*Value is estimated.

**Table 4**
Unidirectional laminate strengths of M30SC/DT120 (quasi-static loading condition).

| Strength | Test method | Test result [MPa] |
|---|---|---|
| $X_T$ | ASTM D3039 | 3010 |
| $X_C$ | ASTM D 6641 | 1020 |
| $Y_T$ | ASTM D 3039 | 39 |
| $Y_C$ | ASTM D 3039 | 138.0 |
| $Z_T$ | ASTM D 3039 | 39 |
| $S_{12}$ | EN 6031 | 95.6 |
| $S_{13}$ ($S_{23}$) | EN 2563 | 77.2 |

### 3.3. FE model validation and verification

#### 3.3.1. Comparison of the force deflection behaviour

A comparison of the force–deflection curves predicted with the FE model and that from the test during the loading phase is shown in Fig. 2. Both were loaded with an indentation force of 5500 N. Fig. 2 shows a good agreement between these two curves, and the errors in the absolute values were also less than 10 %, which indicated that the structural response of the FE model is physically reasonable. The measurement errors in the material elastic and strength property parameters may account for the discrepancies between the FE and test results.

**Table 5**
Test matrix.

| Test group | Number of specimens | $F_{max}$ [N] |
|---|---|---|
| QSI_01 | 1 | 1500 |
| QSI_02 | 1 | 2500 |
| QSI_03 | 1 | 3000 |
| QSI_04 | 3 | 4000 |
| QSI_05 | 3 | 4500 |
| QSI_06 | 3 | 5000 |
| QSI_07 | 3 | 5500 |

#### 3.3.2. Validity of the predicted indentation stress field

To demonstrate the correctness of the indentation stress field predicted by the FE model which considered damage-induced

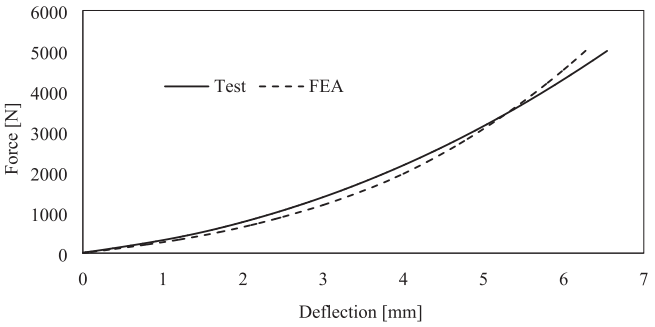


**Fig. 2.** Comparison of the loading phase of the force–deflection curve predicted using the FE model and that obtained from the test, under an indentation force of 5000 N.

degradation in material mechanical properties, the projected delamination lengths $L_{45^\circ}$ and $L_{-45^\circ}$, as defined in Fig. 6 (the associated coordinate system is shown in Fig. 4), were separately predicted using the FE model combined with the Hashin-type and Lee criteria (see Table 2). Because there are generally multiple delaminations along the considered directions, the delamination lengths should be a superposition of several single delamination lengths in these directions. To facilitate the predictions, the delamination lengths $L_{45^\circ}$ and $L_{-45^\circ}$ are approximated as the maximum lengths among all the single delaminations in the 45° and −45° fibre directions:

$$L_\Theta = \max\{l_{\Theta 1}, l_{\Theta 2} \cdots l_{\Theta n}\}, \Theta = \{45^\circ, -45^\circ\}$$

where $l_{\Theta n}$ is the maximum delamination length at the $n^{th}$ ply interface along the fibre direction Θ, and the interface closest to the indented specimen's surface is considered the 1st interface.

To demonstrate how the value of $l_{\Theta n}$ can be determined with the indentation stress field, the determination of the delamination length of the 13th ply interface in the −45° fibre direction (i.e. $l_{-45^\circ 13}$) under an indentation force of 4000 N is employed as an example here. Hence, the corresponding stress distributions were obtained using the FE model (Fig. 3). Fig. 3 shows that the stress distributions had the characteristics that the dominant normal stress was $\sigma_{11}$ and the dominant shear stress was $\sigma_{13}$. According to the simulation results, it is worth noting that under different indentation forces, the stress distributions along the fibre directions at different ply interfaces had similar features to those shown in Fig. 3.

Using the Hashin-type [34] and Lee [35] delamination failure criteria, the stress distributions shown in Fig. 3 can be transformed into curved profiles (Fig. 5). As shown in Fig. 5, the value of $l_{-45^\circ 13}$ is equal to the straight-line distance in the x-axis direction between the points on the Hashin-type and Lee delamination failure criterion curves, with a value of 1 (Fig. 5). Using the same method as for the determination of $l_{-45^\circ 13}$ under an indentation force of 4000 N, the delamination lengths along other fibre directions of the 13th ply interfaces or along any fibre direction at different ply interfaces with different indentation forces can also be determined. After obtaining the value of $l_{\Theta n}$ for different indentation forces using Eq. (1), the projected delamination length along the fibre direction ($L_\Theta$) can also be determined. Finally, the predicted delamination lengths were compared with the experimentally measured values, the results are shown in Fig. 6.

Fig. 6 shows that the predicted and experimentally measured delamination lengths agreed considerably well with the use of these two criteria, both with prediction errors of less than 10 %. Note that in the determination of $l_{\Theta n}$, the regions where $\sigma_{33}$ less than 0 were not considered, because some researchers, such as Davies and Zhang [48], Hou et al. [49], and Esrail and Kassapoglou [50], suggested that the delamination is difficult to initiate and propagate in areas in which the out-of-plane stress $\sigma_{33}$ is negative or mostly negative for a composite laminate under out-of-plane concentrated loading. The good agreement between the simulation and test results shown in Fig. 5 supports this assumption when determining $l_{\Theta n}$. This is also the reason for the discontinuities of the Hashin-type and Lee delamination failure criterion curves as shown in Fig. 5. In addition, the good match between the experimental measured and predicted delamination lengths indicates that the proposed FE model can reliably determine the indentation stress field. These results suggest that the proposed FE model accurately captures the main characteristics of the indentation stress field. Moreover, the statement that the influence of the indentation delaminations on the global indentation stress field distribution can be neglected is confirmed.

However, new questions arise: exactly what stress component/-combination drives the delamination growth along the considered directions and what is/are the associated delamination growth threshold(s)? Both the Hashin-type and Lee failure criteria failed

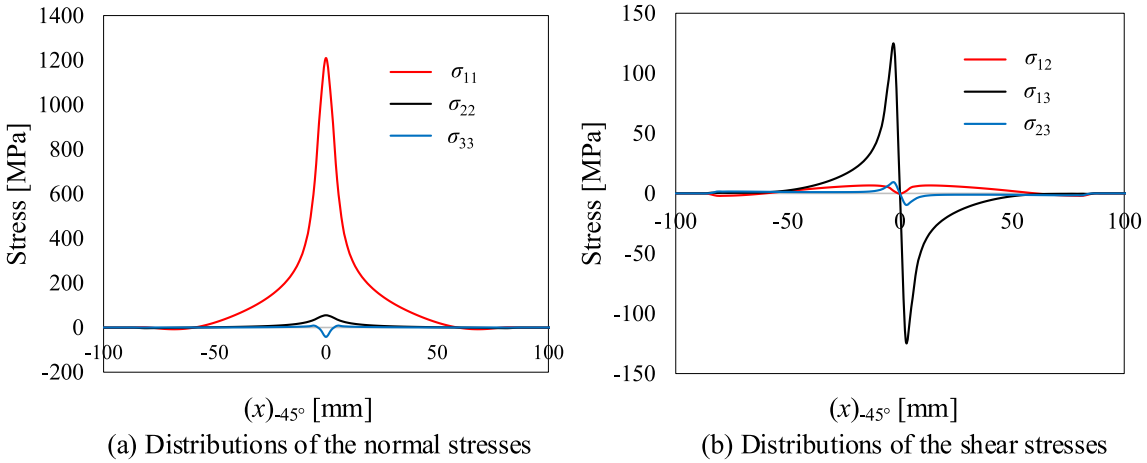


**Fig. 3.** Normal and shear stress distributions at the 13th ply interface under the indentation force of 4000 N in the −45° fibre direction (i.e. along the path that coincides with the $(x)_{-45^\circ}$-axis as shown in Fig. 4) predicted by the FE model.

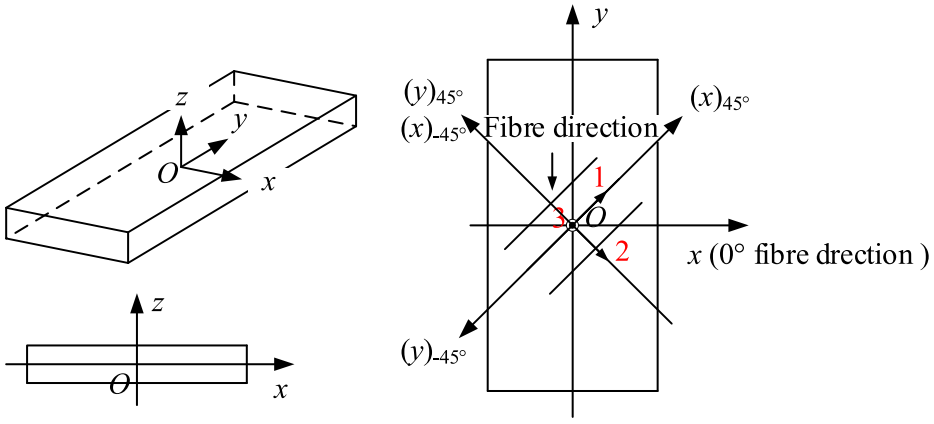


**Fig. 4.** Cartesian coordinate systems used in this study: global coordinate systems (black x-y-z, $(x)_{45°}$-$(y)_{45°}$-z and $(x)_{-45°}$-$(y)_{-45°}$-z) and local coordinate system (red 1–2-3). (For interpretation of the references to colour in this figure legend, the reader is referred to the web version of this article.)

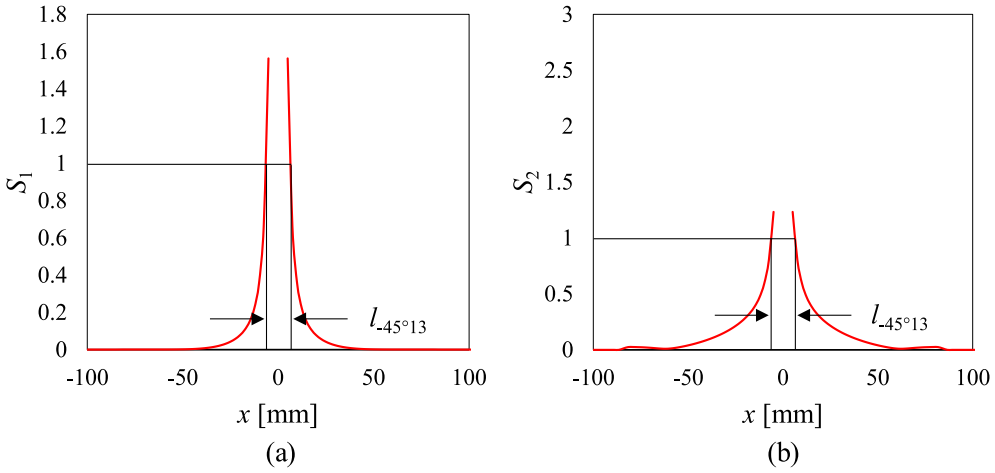


**Fig. 5.** Determination of the delamination length at the 13th ply interface with the indentation force of 4000 N in the −45° fibre direction based on the predicted stresses shown in Fig. 3, $\sigma_{33} \geq 0$: (a) $S_1 = (\sigma_{33}/Z_T)^2 + (\sigma_{13}/S_{13})^2 + (\sigma_{23}/S_{23})^2$, (b) $S_2 = \sqrt{(\sigma_{12}^2 + \sigma_{13}^2)}/S_{13}$.

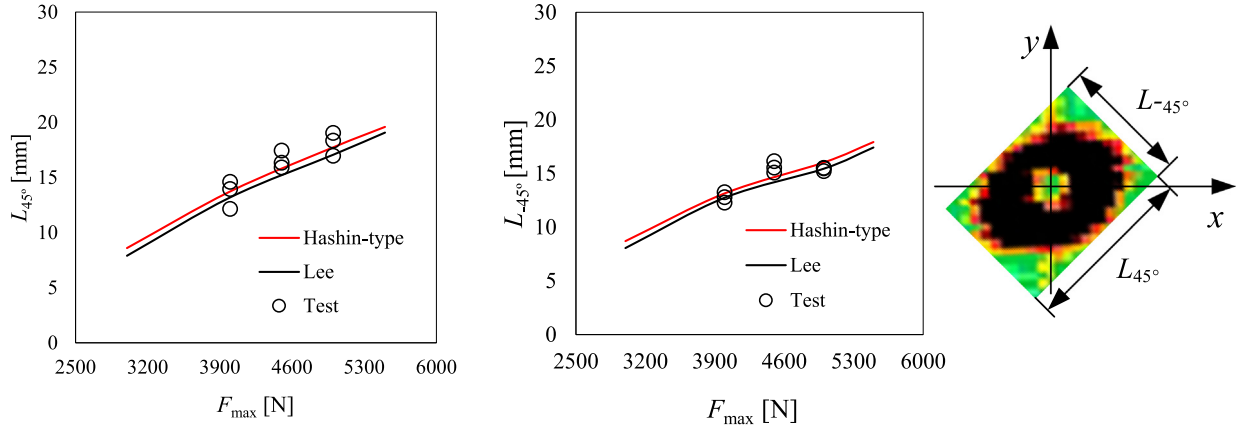


**Fig. 6.** Comparison of the predicted and experimentally measured delamination lengths; the utilized indentation stress field was determined using the FE model; the associated coordinate system is shown in Fig. 4.

to answer these two questions. In addition, because that the common part of these two criteria is $\sigma_{33}/Z_T$ or $\sigma_{13}/S_{13}$, in essence, these two combinations should be most relevant for delamination growth along the considered directions. The delamination failure criteria can only be simplified after a full understanding of which stress component/combination dominates the delamination growth and ignoring less relevant stress component(s).

## 4. Results and discussion

### 4.1. Features of quasi-static indentation damage morphologies

From the perspective of material strength, delamination growth in an indented composite laminate is considered to be driven by certain stress combination(s). By correctly determining the stress

states at the delamination fronts and determining which stress combination(s) is/are physically related to the fracture morphologies of the delamination fronts, the critical stress combination(s) for delamination growth can be determined. In this section, the damage morphologies (i.e. C-scan projected damages and cross-sectional damages) of the composite laminates are first examined to obtain a general understanding of the basic features of indentation damage. Subsequently, the relationship between the stress states and the fracture morphologies of the delamination fronts are investigated.

### 4.2. C-scan damage morphologies

The projected indentation C-scan damage refers to the superposition of several single delaminations at different interfaces. As shown in Fig. 7, the shapes of the C-scan damages were not perfect circles, although the laminated composite plates were a quasi-isotropic with symmetric layup. In addition, no damage was observed at the centre of the C-scan records. These undamaged areas corresponded to regions of high out-of-plane compression and low out-of-plane shear zones during the loading process, prohibiting the initiation of delamination damage. This was demonstrated by Esrail and Kassapoglou [50], who calculated the stresses inside the contact zone. Moreover, C-scan damage was initiated when the indentation force reached between 1500 and 2500 N and then propagated outwards along the radius of the ring-shaped damage zones.

### 4.3. Cross-sectional damage morphologies

C-scan damage detection can only provide the external contours of superimposed delaminations. Therefore, the damaged specimens were sectioned, and internal damage was observed through microscopy. The processed cross-sectional damage is shown in Fig. 8, where the delamination fronts were marked with red numbers, and the interfaces containing the delamination fronts are summarised in Table 6.

Fig. 8 shows that when $F_{max}$ was not greater than 3000 N, no delamination was observed in the interfaces above the mid-plane. The delaminations immediately beneath the mid-plane had the largest size. Another distinguishing feature was that all the delaminations grew in an almost proportional to the indentation force and stopped at the interfaces where the lower ply (away from the indented surface) fibre orientation was 0° (Table 6).

### 4.4. Stress states of the delamination fronts

Damage information can be learned at an empirical level. To step further, the stress states at the points where delaminations arrested were investigated through the FE model described in Section 2.1. The specific steps of this approach are as follows:

As shown in Fig. 8, the red centrelines of the samples correspond to the z-axis of the Cartesian coordinate system shown in Fig. 4, and the cross-sections of the samples are parallel to the x–z plane. Using this coordinate system, the coordinates of the delamination fronts can be determined.

The stress states of the delamination fronts can be determined by tracking points with the same coordinates in the FE model. Note that he stresses in the layer surface nodes adjacent to the delamination fronts are used to approximate the stress states.

This method may raise concerns that cracks at the delamination front may close during/after the unloading phase (crack closure), and the delamination may become shorter owing to the crack closure. This affects the measurement accuracy of the delamination lengths, which is crucial for determining the stress state at the delamination front. However, observations of the crack closure indicated that the location of the closed crack tip can still be distinguished [51,52]. In addition, detailed variations in the stress field at the crack front owing to crack closure were not the focus of this study. Therefore, the crack closure was not considered in this study.

Fig. 8 shows that there were 26 delaminations in total, with their fronts separately distributed at different interfaces. Six delamination fronts were distributed at interfaces L05/L06, ten at interfaces *L*10/*L*11, and ten at interfaces L14/L15. To facilitate the analysis of these 26 stress state groups, the average stress components were considered. The average stress component is defined as follows:

$$\bar{\sigma}_{ij} = \sum_{i}^{3} \sum_{j}^{3} \sigma_{ij} / N_{\psi}$$

where $\sigma_{ij}$ is the corresponding delamination front stress and $N_{\psi}$ is the number of considered delamination fronts at the same interface; for example, $N_{\psi}$ is 6 when the delamination fronts at interfaces L05/L06 are considered.

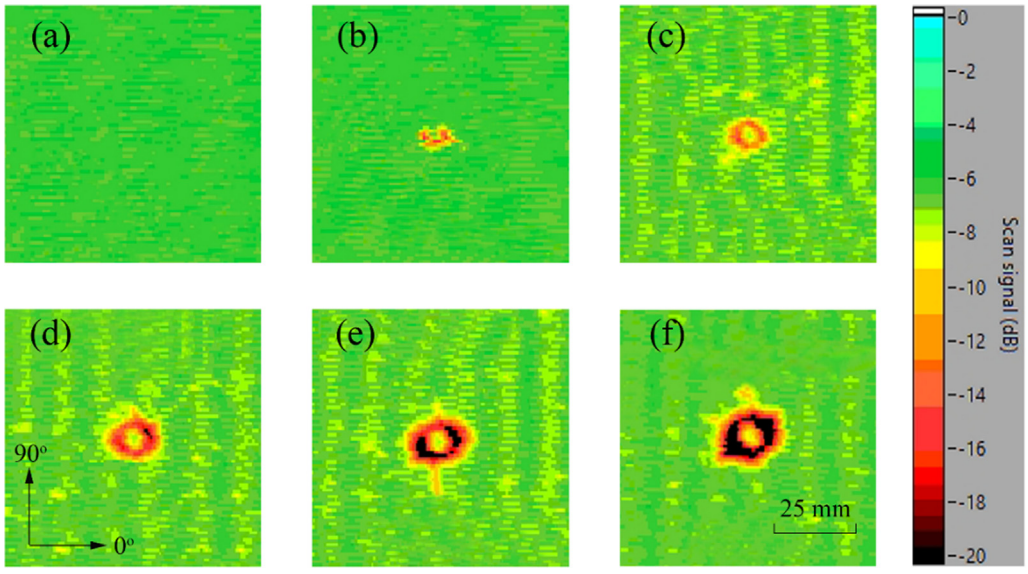


**Fig. 7.** C-scan damages of the specimens with different maximum indentation forces: (a) QSI_01, $F_{max}$ = 1500 N, (b) QSI_02, $F_{max}$ = 2500 N, (c) QSI_03, $F_{max}$ = 3000 N, (d) QSI_04, $F_{max}$ = 4000 N, (e) QSI_06, $F_{max}$ = 5000 N, and (f) QSI_07, $F_{max}$ = 5500 N.

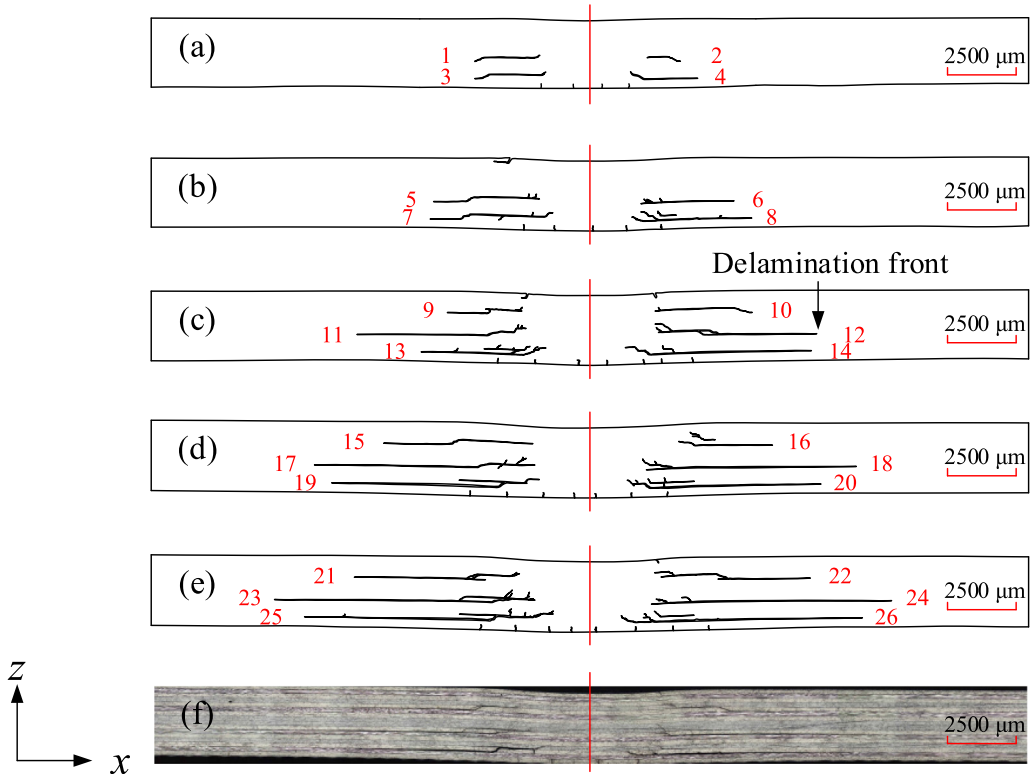


**Fig. 8.** Cross-sectional damage morphologies with different maximum indentation forces: (a) QSI_02, $F_{max}$ = 2500 N, (b) QSI_03, $F_{max}$ = 3000 N, (c) QSI_04, $F_{max}$ = 4000 N, (d) QSI_06, $F_{max}$ = 5000 N, (e) QSI_07, $F_{max}$ = 5500 N, and (f) original damage micrograph of case (e); the specimens were sectioned along the red line as shown in Fig. 1(d). (For interpretation of the references to colour in this figure legend, the reader is referred to the web version of this article.)

**Table 6**
Interfaces containing delamination fronts of the cross-sections shown in Fig. 8.

| Interface | Delamination front |
|---|---|
| L05/L06 (45°/0°) | 9, 10, 15, 16, 21, 22 |
| *L*10/*L*11 (-45°/0°) | 1, 2, 5, 6, 11, 12, 17, 18, 23, 24 |
| L14/L15 (-45°/0°) | 3, 4, 7, 8, 13, 14, 19, 20,25, 26 |

Finally, the average stress components were calculated; their values are summarised in Table 7, and the corresponding standard deviations are listed in Table 8. Because the signs of the shear stress components were opposite on different sides of the centre-line of the contact area, the average of their absolute values was considered. Table 7 shows that the stress states at the delamination fronts are three-dimensional. In terms of stress amplitude, $\sigma_{xx}$ was dominant among all the normal stresses, and for all the absolute shear stress components, $|\sigma_{xz}|$ was the largest. However, the delamination growth may not be primarily driven by the combination of in-plane tensile stress $\sigma_{xx}$ and out-of-plane shear stress $\sigma_{xz}$, and the influences of other stress components are negligible. The ratio of different stresses to their corresponding strengths should be compared to determine which stress component(s) dominate in controlling delamination growth.

Therefore, the stress-to-strength ratios of different delamination fronts were calculated using the strength parameters listed in Table 4, and the corresponding stress-to-strength ratios are summarised in Table 9. Table 9 shows that among all the shear stress-to-strength ratios, $\left|\bar{\sigma}_{xz}\right|/S_{xz}$ was dominant, and its value at different interfaces was close to 1. Thus, other shear stress components could be neglected because of their negligible stress-to-strength ratios. For the normal stress-to-strength ratios, $\bar{\sigma}_{xx}/X_t$ of all delamination fronts was considerably small compared with the other two ratios, although $\sigma_{xx}$ has the largest magnitude. Because $\sigma_{yy}$ is always perpendicular to the x-axis direction (Fig. 8), this stress is considered to not contribute to delamination propagation along this direction. Thus, it can be concluded from Table 9 that the delamination growth along the x-axis direction is primarily driven by the out-of-plane shear stress $\sigma_{xz}$, whereas the influences of other stress components can be neglected.

### 4.5. Two basic microscopic delamination-growth mechanisms

The stress analysis performed using the FE method showed that delamination growth along the x-axis direction is primarily driven by the out-of-plane shear stress $\sigma_{xz}$, owning to the fact that $\left|\bar{\sigma}_{xz}\right|/S_{xz}$ of different delamination fronts is close to 1. However,

**Table 7**
Stress states of the delamination fronts at different interfaces (average values).

| Delamination | $\bar{\sigma}_{xx}$ [MPa] | $\bar{\sigma}_{yy}$ [MPa] | $\bar{\sigma}_{zz}$ [MPa] | $\left\|\bar{\sigma}_{xy}\right\|$ [MPa] | $\left\|\bar{\sigma}_{xz}\right\|$[MPa] | $\left\|\bar{\sigma}_{yz}\right\|$ [MPa] |
|---|---|---|---|---|---|---|
| L05/L06 | 322.06 | −16.49 | 9.80 | 2.81 | 65.36 | 3.04 |
| *L*10/*L*11 | 393.82 | 16.80 | 8.48 | 1.17 | 70.44 | 1.92 |
| L14/L15 | 524.15 | 47.91 | 9.11 | 3.12 | 73.89 | 5.38 |

**Table 8**
Standard deviations of the delamination front stress components.

| Delamination | $\sigma_{xx}$ [MPa] | $\sigma_{yy}$ [MPa] | $\sigma_{zz}$ [MPa] | $\lvert\sigma_{xy}\rvert$ [MPa] | $\lvert\sigma_{xz}\rvert$ [MPa] | $\lvert\sigma_{yz}\rvert$ [MPa] |
|---|---|---|---|---|---|---|
| L05/L06 | 74.98 | 1.64 | 2.99 | 0.87 | 12.82 | 2.23 |
| *L*10/*L*11 | 48.45 | 2.63 | 3.03 | 1.05 | 7.82 | 1.93 |
| L14/L15 | 64.38 | 6.18 | 3.58 | 2.44 | 16.26 | 1.98 |

**Table 9**
Stress-to-strength ratios of different delamination fronts.

| Stress/strength ratio | L05/L06 | *L*10/*L*11 | L14/L15 |
|---|---|---|---|
| $\bar{\sigma}_{xx}/X_t$ | 0.11 | 0.13 | 0.18 |
| $\bar{\sigma}_{yy}/Y_t$ | 0 | 0.43 | 1.23 |
| $\bar{\sigma}_{zz}/Z_t$ | 0.29 | 0.24 | 0.27 |
| $\lvert\bar{\sigma}_{xy}\rvert/S_{xy}$ | 0.03 | 0.012 | 0.032 |
| $\lvert\bar{\sigma}_{xz}\rvert/S_{xz}$ | 0.86 | 0.93 | 0.98 |
| $\lvert\bar{\sigma}_{yz}\rvert/S_{yz}$ | 0.04 | 0.025 | 0.069 |

the result is still not convincing unless it is demonstrated that the delamination growth mechanism(s) along this direction is/are physically related to or primarily driven by $\sigma_{xz}$. In this section, two basic microscopic delamination growth mechanisms along the x-axis direction and their relationships with the out-of-plane shear stress $\sigma_{xz}$ are discussed in detail. Hence, it is necessary to first understand the deformation behaviour of the indented composite laminate.

### 4.6. Plate deformation under out-of-plane indentation loading

There are major differences between thin and thick laminates under out-of-plane impact loading, primarily owing to stress wave propagation [53]. The stress waves travel a longer distance through thick laminates than through thin ones; and thus, they dissipate more in former laminates. This means that for typical energy levels, most of the damage is confined to the top half of a thick laminate, as opposed to damages being present everywhere in a thin laminate. However, stress waves do not represent the loading process for a composite laminate under quasi-static indentation; instead, the major discrepancy between thin and thick laminates is their deformation. Different deformations induce different stress fields and indirectly result different damage patterns.

Generally, for a composite laminate under out-of-plane indentation loading, as shown in Fig. 9, plate deformations can be further divided into contact and bending deformations [40,54]. The aspect ratio [55] was adopted from the literature to distinguish thin and thick plates from a geometrical perspective, but this ratio alone cannot precisely describe the plate deformation under indentation loading because the deformations are also significantly affected by the applied load.

In this study, the diameter of the indenter was 25 mm, which was negligibly small compared with the dimensions of the exposed specimen's surface (120 mm in width and 215 mm in length). The rotation angle $\theta$ was used to quantify the extent of the bending plate deformation, and its definition is shown in Fig. 10. The value of $\theta$ for laminates with different indentation forces was calculated using the FE model, and the results are summarised in Table 10.

Table 10 shows that $\theta$ did not change significantly as different indentation loads were applied to the centre of the plate: it varied from 6° to 8°. More importantly, further investigation has shown that $\theta$ is important in the formation of delamination front cracks. It changes the orientations of stress components (associated with the fixed global x–y–z coordinate system) at the delamination front relative to the resin rich-ply interfaces, particularly for the out-of-plane shear stress $\sigma_{xz}$ (Fig. 11) which is considered the major driving force for delamination growth along the x-axis direction. The magnitude of $\theta$ relates to how $\sigma_{xz}$ drives delamination growth.

### 4.7. Opening crack-dominated delamination failure

At the global level, the delaminations created due to out-of-plane concentrated loading are pure Mode II type [56], but at the microscopic level, the fractographic analyses indicated that the fronts of these macroscopic Mode II delaminations can be either opening crack-dominated or sliding crack-dominated, which can assist in better understanding the micro-mechanisms of delamination growth. The failure process of opening crack-dominated delaminations can be divided into three distinct phases: crack nucleation (stage I), crack growth (stage II), and tensile breakage (stage III). In the crack nucleation stage (stage I), as shown in Fig. 12(A), the opening cracks induced by $\sigma_{xz}$ first emerge in the central area of the resin-rich zone. A photomicrograph of the crack-nucleation stage is shown in Fig. 12(a). The effects of other stresses on the crack formation in this stage are negligible. The second stage is the crack growth stage (stage II, Fig. 12(B)), which is characterised by increased crack density and enlarged crack sizes. The corresponding microscopic image of this stage is shown in Fig. 12(b). Similar to the first stage, the driving force for the crack growth is $\sigma_{xz}$. The last stage (stage III) is the tensile failure stage, where $\sigma_{xx}$, $\sigma_{zz}$, and $\sigma_{xz}$ take effect simultaneously. In this stage, tensile breakage caused by $\sigma_{xx}$ occurs in the resin between two adjacent cracks (as indicated by the blue line in Fig. 12(C)), whereas $\sigma_{xz}$ and $\sigma_{zz}$ result in further expansion of the formed cracks along the maximum principal stress and z-axis directions, respectively. A micrograph of this stage is shown in Fig. 12(c). A shark teeth breakage further demonstrates this delamination growth mode (Fig. 12(d)).

In summary, $\sigma_{xx}$, $\sigma_{zz}$, and $\sigma_{xz}$ participate in the propagation of delamination in this mode along the x-axis direction. $\sigma_{xz}$ induces cracks at the delamination front and then expands their density and size, while $\sigma_{zz}$ enlarges the crack size and $\sigma_{xx}$ acts to fail the resin between two adjacent cracks in the final stage. The operation of $\sigma_{xz}$ can be explained through the maximum principal stress theory [56]; therefore, the shear cracks in the resin-rich area are essentially tensile failures [57,58]. Thus, crack failures at the delamination front at each stage belong to the opening type, and the microscopic mechanism of this delamination propagation can be considered opening crack-dominated.

### 4.8. Sliding crack-dominated delamination failure

Sliding crack-dominated delamination propagation is also primarily driven by $\sigma_{xz}$, which has only two distinguishable phases: delamination nucleation (stage I) and delamination expansion (stage II). As shown in Fig. 13(A), sliding-type cracks caused by $\sigma_{xz}$ form delamination nucleation. A micrograph that matches this stage is shown in Fig. 13(a). In the delamination expansion stage, delamination nucleation is enlarged under the combined effect of $\sigma_{xx}$, $\sigma_{zz}$, and $\sigma_{xz}$. After these two stages, delamination occurs, and the corresponding fracture image is shown in Fig. 13(b).

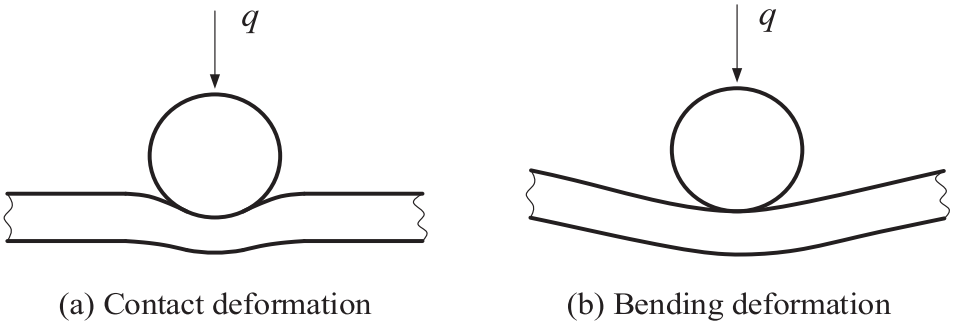


**Fig. 9.** Illustration of two basic deformations of a plate under out-of-plane quasi-static indentation loading.

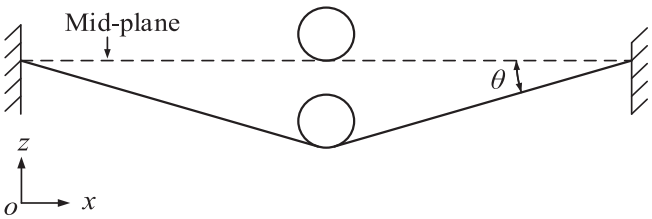


**Fig. 10.** Rotation angle θ, which is defined as the angle between the original location of the line (intersection line of the mid-plane and cross-sectional plane shown in Fig. 8) and that corresponding to the moment when indentation force reaches its maximum.

In summary, the nucleation stage consists of a series of sliding cracks caused by $\sigma_{xz}$, and the basic fracture features of delamination are formed during this stage. Only the distance between the two delamination boundaries is expanded by the combination of $\sigma_{xx}$, $\sigma_{zz}$, and $\sigma_{xz}$ in the subsequent stage. Consequently, this delamination growth was essentially sliding crack-dominated.

The discussed microscopic-level delamination growth mechanisms suggest that the major driving force for delamination growth along the x-axis direction is $\sigma_{xz}$. Although $\sigma_{xx}$ and $\sigma_{zz}$ are also involved in the formation of delaminations, they primarily affect the secondary characteristics of the formed delaminations. $\left|\bar{\sigma}_{xz}\right|/S_{xz}$ of different delamination fronts listed in Table 9 is close to 1, which broadly supports this conclusion. The problem, however, is that $\left|\bar{\sigma}_{xz}\right|/S_{xz}$ was defined using the average absolute shear stresses, which may be misleading considering that $|\sigma_{xz}|/S_{xz}$ at some delamination fronts may significantly deviate from 1.

Therefore, the conclusion that the delamination growth along the x-axis direction is primarily driven by $\sigma_{xz}$ must be further demonstrated. Hence, the values of $|\sigma_{xz}|/S_{xz}$ for all the delamination fronts were evaluated, and the results are summarised in Fig. 14. Fig. 14 shows that the variation in $|\sigma_{xz}|/S_{xz}$ was considerably stable for different delamination fronts; the ratios were close to 1 with acceptable errors (most of the errors in absolute values are less than 10 %). These errors are primarily associated with the determination of delamination front coordinates. In practice, it is impossible to section the damaged specimens exactly along the expected path (red line in Fig. 1(d)); thus, the corresponding errors are unavoidable. Grinding and polishing during sample preparation may adversely affect the original damage morphology. However, even if the specimens are precisely cut and no new damage is introduced, measuring the delamination front stresses exactly corresponding to the delamination growth load is still impossible. The $\sigma_{xz}$ mechanism described here occurs before complete formation of observable delaminations. These factors cause the stresses to actually be taken near the load at which delamination took place, resulting in $|\sigma_{xz}|/S_{xz}$ generally deviating from 1. However, with the $|\sigma_{xz}|/S_{xz}$ variations shown in Fig. 14, the argument that delamination growth along the x–axis direction is primarily driven by $\sigma_{xz}$ is well supported by these results.

**Table 10**
Rotation angle θ of the plates predicted by the FE model.

| Specimen | QSI_02 | QSI_03 | OSI_04 | OSI_06 | QSI_07 |
|---|---|---|---|---|---|
| θ [°] | 6 | 6 | 7 | 7 | 8 |

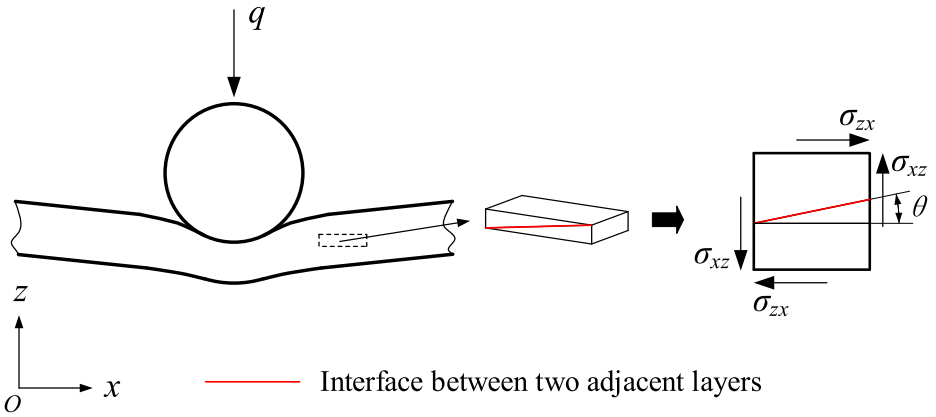


**Fig. 11.** Illustration of the orientation of out-of-plane shear stress $\sigma_{xz}$ relative to the resin-rich interface with the consideration of rotation angle.

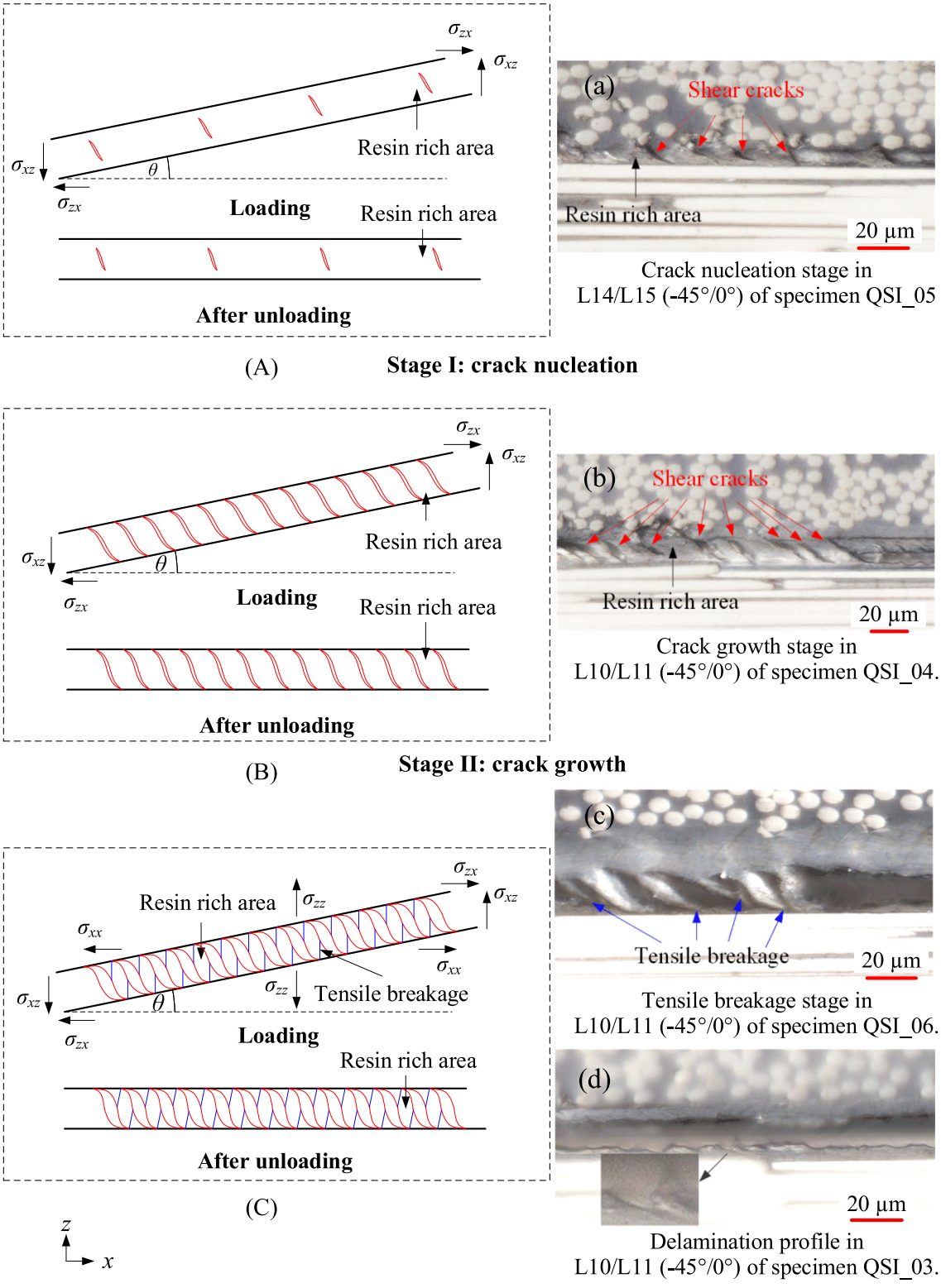


**Fig. 12.** Formation process of opening crack-dominated delamination and its driving forces; the resin-rich area refers to the considered delaminated interfaces.

### *4.9. Generalization of the delamination failure principle*

It has been demonstrated that the delamination growth along the x–axis direction (Fig. 8) can be characterised by the out-of-plane shear stress $\sigma_{xz}$ along. The corresponding delamination growth criterion can be formulated as.

$$\left(\frac{\sigma_{xz}}{S_{xz}}\right)^2 = 1$$

In addition, experiments indicated that single-impact delaminations distributed at different interfaces are generally peanut-like [4,40,48,50,59], with their major axes parallel to the fibre

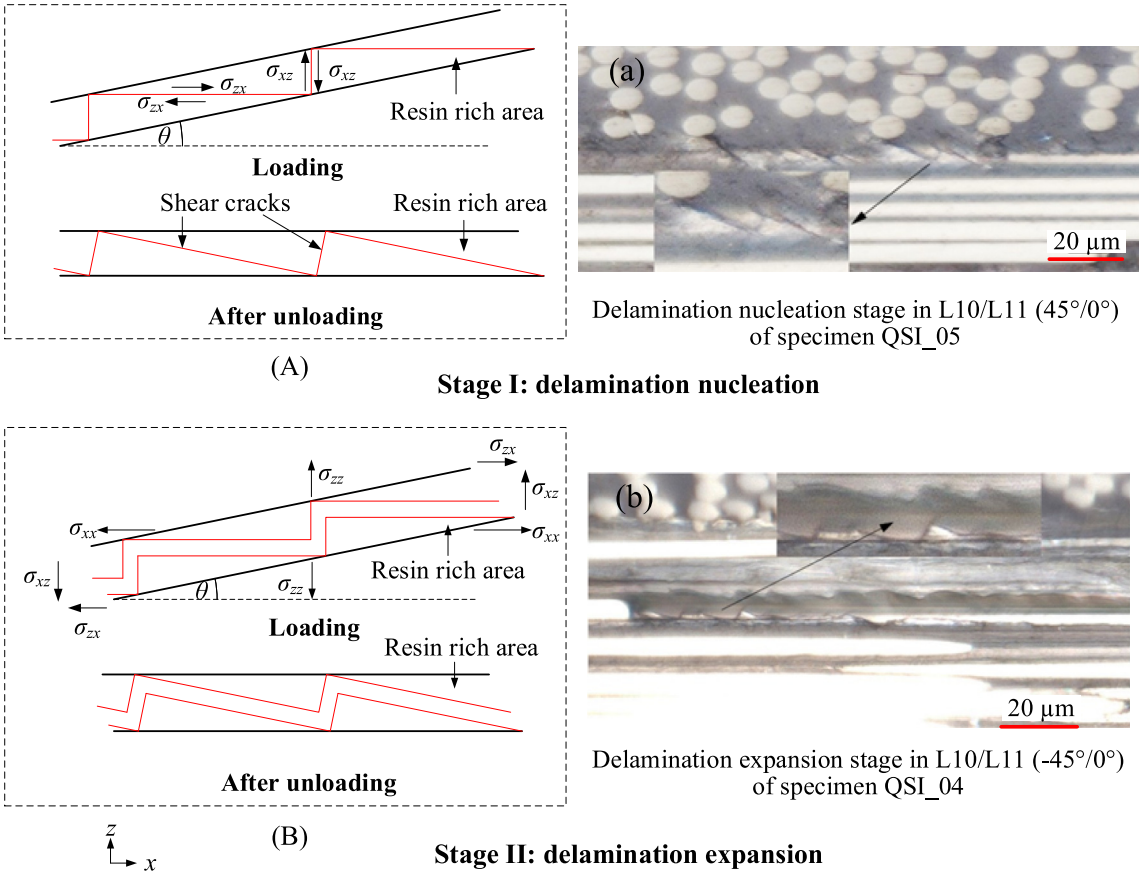


**Fig. 13.** Formation process of sliding crack-dominated delamination and this driving forces; the resin-rich area refers to the considered delaminated interfaces.

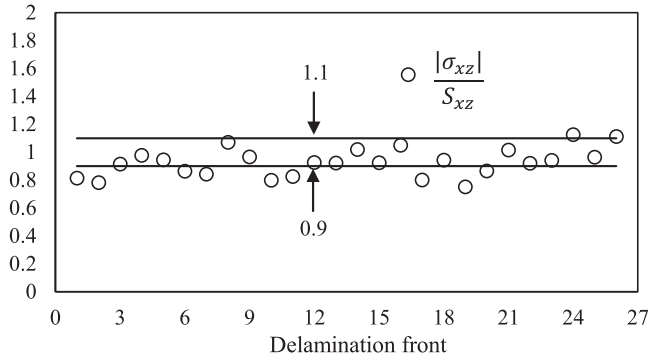


**Fig. 14.** Variations in $\sigma_{xz}/S_{xz}$ for different delamination fronts shown in Fig. 8.

directions of the lower plies (i.e. plies further away from the impact site) at each ply interface [19,60]. These results were observed from various low-velocity impact tests and indicate that delamination growth along their major axes coincides with the lower ply fibre orientations of the delaminated interfaces, where, for any ply interface of interest, 'lower ply' refers to the ply farther away from the impact site. Although static indentation and low-velocity impact do not always have a one-to-one correspondence, it is reasonable to conclude that the growth of indentation delaminations follows a pattern similar to that of low-velocity impact delamination.

It can, therefore, be assumed that a single indentation delamination would also have a peanut-like shape, and its major axis would be aligned with the lower fibre directions at the considered interfaces. With this assumption, the composite laminate with a quasi-isotropic layup $[45/0/-45/90]_{2s}$ used in this study should have a delamination distribution (Fig. 15). Subsequently, if the damaged specimens are sectioned along the red line shown in Fig. 1(d), which perpendicularly intersects with the centreline of the contact area and is parallel to the x-axis, only the delaminations whose major axes coincide with the x-axis can be observed. The damage information transferred from Fig. 8 shows that delamination fronts are always observed in the interfaces with a lower ply fibre direction of 0° (Table 6), which supports this proposed assumption.

To further validate this assumption, the damaged specimens with indentation forces of 4000, 4500, and 5500 N were sectioned along the blue line (Fig. 1(d)), which was at a 45° angle with the red

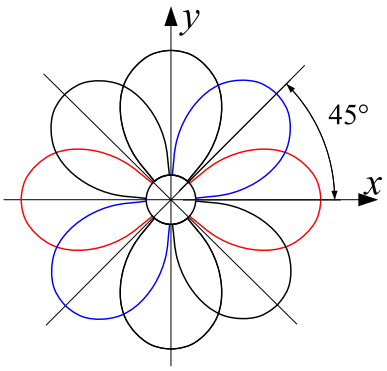


**Fig. 15.** Hypothetical indentation delamination distributions in composite laminates with quasi-isotropic layup $[45/0/-45/90]_{2s}$.

cutting path. The corresponding delamination morphologies are shown in Fig. 16, and the interfaces containing the delamination fronts are listed in Table 11.

Fig. 16 and Table 11 show that most of the delamination fronts were observed at the interfaces where the lower ply fibre direction was 45°. Therefore, this indirectly demonstrated that the indentation delaminations also consist of single peanut-like delaminations with their major axes parallel to the lower ply fibre orientations of the delaminated interfaces. However, to directly demonstrate this point, a thorough investigation using the thermal deply technique of polymer composites [61] is necessary.

In addition, the growth of single-indentation delaminations along their major axes should follow the same principle as the x-axis direction and be driven by the same stress. Otherwise, it is impossible to form similar single delaminations with their major axes parallel to the lower fibre directions of the delaminated interfaces. Consequently, the delamination growth criterion shown in Eq. (3) which was developed based on the delamination propagation along the x-axis direction (0° fibre direction), should also be applicable to delamination growth along other fibre directions. The general form of the delamination failure criterion is as follows:

$$\left(\frac{\sigma_{13}}{S_{13}}\right)^2 = 1$$

where $\sigma_{13}$ is the out-of-plane shear stress in the plane containing the centreline of the contact area and parallel to the lower fibre direction of the considered interface, and $S_{13}$ is the out-of-plane shear strength of the unidirectional laminates, which is the same as $S_{xz}$ in this study.

To validate the concise Hashin-type delamination failure criterion expressed in Eq. (4), the delamination lengths, $L_{45°}$, $L_{90°}$, and $L_{-45°}$ of the damaged specimens were measured, and the definitions of these delamination lengths are shown in Fig. 17. The specimens were separately loaded with indentation forces of 4000, 4500, 5000 and 5500 N. Meanwhile, the delamination lengths along the considered fibre directions (i.e. 45°, 90°, and −45° fibre directions) were predicted by incorporating the delamination growth criterion with the indentation stress fields determined by the FE model, and the determination of the delamination lengths similar to those shown in Eq. (1).

**Table 11**
Interfaces containing delamination fronts in the cross-sections shown in Fig. 16.

| Interface | Delamination fronts |
|---|---|
| L03/L04 (0°/-45°) | 28 |
| L04/L05 (90°/45°) | 27, 33, 34, 39, 40 |
| L11/L12 (0°/45°) | 29, 30, 35, 36, 41, 42 |
| L15/L16 (0°/45°) | 31, 32, 37, 38, 43, 44 |

The 0° fibre direction delamination lengths were not considered because the delamination growth criterion was developed based on observations of delamination propagation along this direction. Finally, the predicted delamination lengths were obtained and compared with the measured delamination lengths; the results are shown in Fig. 17. Fig. 17 shows good agreement between the delamination lengths predicted by the FE model using the proposed stress-based delamination growth criterion and the measured results. Noise in the ultrasonic C-scan record is considered to be the major error source for determining the delamination lengths. To reduce measurement errors, more advanced non-destructive damage detection techniques, such as μ-CT, are necessary.

Finally, the research object of developing a simplified, valid, and physically sound delamination failure criterion to predict the projected delamination areas of composite laminates under out-of-plane quasi-static indentation loading was achieved. Compared with the Hashin-type delamination criterion shown in the first item of Table 2 (to the best of the authors' knowledge, this criterion was first reported by Shokrieh et al. [62] in 1996 and then named the Hashin-type delamination criterion by Tserpes et al. [34] in 2001), the proposed delamination failure criterion has only one stress component and strength parameter and can be considered a concise version of the Hashin-type delamination failure criterion. Generally, no delamination can be observed at the interface between plies with the same fibre orientation [60], and the developed delamination failure criterion is not considered applicable to this special case. It is noteworthy that the proposed model has some advantages over other approaches, such as those using cohesive zone models: it involves fewer material parameters, is computationally efficient, and has good prediction accuracy; it is physics-based and does not require the use of multiple experimentally

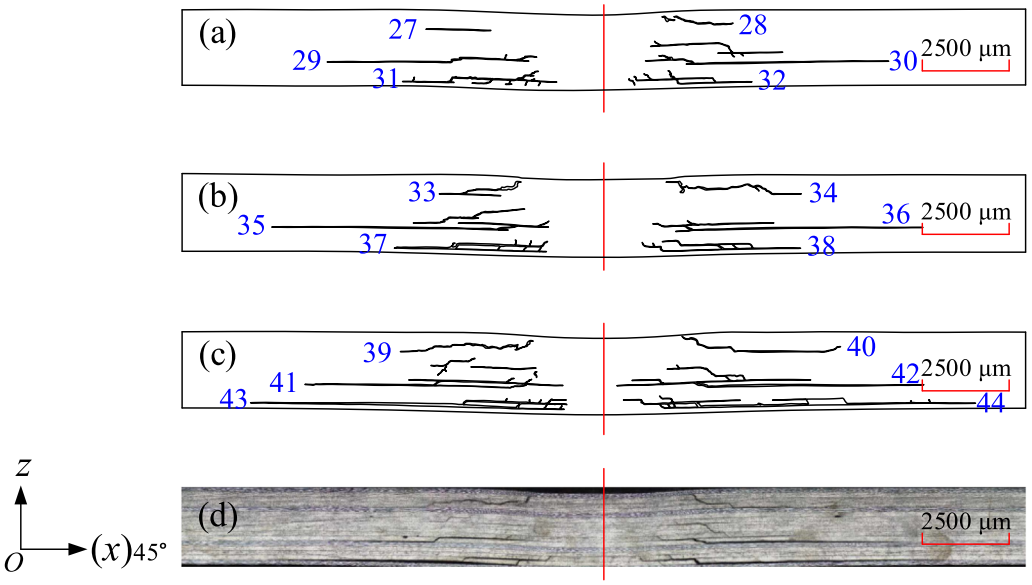


**Fig. 16.** Cross-sectional damage morphologies with different maximum indentation forces: (a) QSI_04, $F_{max}$ = 4000 N, (b) QSI_05, $F_{max}$ = 4500 N, (c) QSI_07, $F_{max}$ = 5500 N, and (d) original damage micrograph of case (c); the specimens were sectioned along the blue line as shown in Fig. 1(d). (For interpretation of the references to colour in this figure legend, the reader is referred to the web version of this article.)

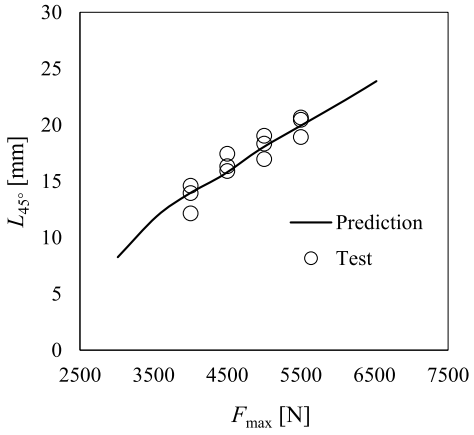


(a) Comparison of the delamination length $L_{45°}$

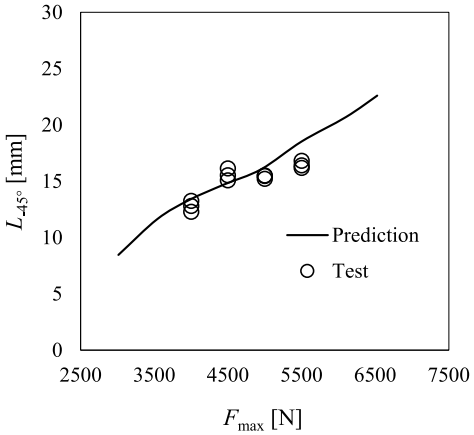


(b) Comparison of the delamination length $L_{-45°}$

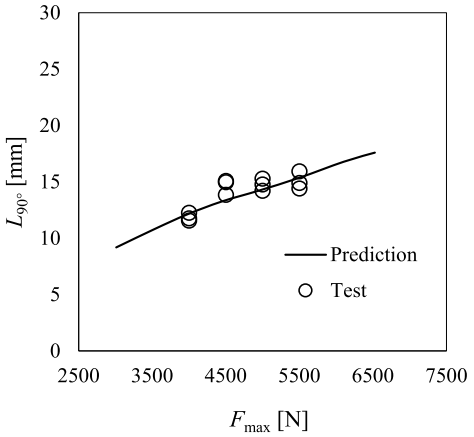


(c) Comparison of the delamination length $L_{90°}$

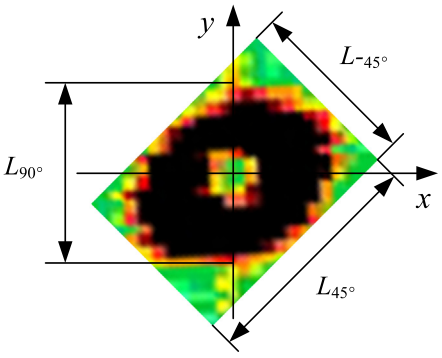


**Fig. 17.** Comparisons of the predicted and experimentally measured delamination lengths.

determined curve-fitted parameters. In addition, because cohesive elements are not necessary, the proposed method does not have convergence or mesh sensitivity problems associated with the application of such elements.

## 5. Conclusions

In this study, the delamination growth behaviour of multidirectional CFRP laminates under out-of-plane quasi-static indentation loading with fully clamped boundary conditions was investigated. This study highlighted that the specific shear stress that drives the delamination growth in the fibre directions is $\sigma_{13}$ (the local coordinate system is associated with the lower ply fibre orientation; the lower ply here is referred to as the ply further away from the indentation site of any two adjacent layers with different fibre orientations), and the relevant delamination growth threshold is $S_{13}$. These two parameters are not considered simultaneously in some commonly used delamination criteria which are shown in Table 2. The main conclusions of this study are as follows:

- Along the 0° fibre direction, two basic microscopic delamination growth mechanisms, namely opening crack-dominated and sliding crack-dominated delamination failures, were distinguished according to the fracture features of the microscopic delamination. The delamination front of the former consists of a series of opening cracks, whereas that of the latter consists of a combination of several sliding cracks. Both are induced by out-of-plane shear stresses $\sigma_{13}$.
- A concise Hashin-type delamination failure criterion is proposed based on the investigation of delamination growth along the 0° fibre direction of quasi-isotropic laminates. This criterion is applicable to predicting the delamination growths along the lower fibre directions of the considered interfaces. Indentation delamination propagation along the fibre directions can be successfully predicted by incorporating this delamination failure criterion with the FE model.

Note that this study only investigated large deformed indented composite laminates, and more research is required to show that the proposed delamination failure criterion is also valid for other cases, such as thick laminates with high resistance to indentation deformation. To generalise the proposed delamination prediction method to other complex loading conditions, double-cantilever beam (DCB) and/or end-notched flexure (ENF) tests are necessary.

## Data availability

Data will be made available on request.

## Declaration of Competing Interest

The authors declare that they have no known competing financial interests or personal relationships that could have appeared to influence the work reported in this paper.

## Acknowledgement

The authors gratefully acknowledge the financial support from the China Scholarship Council (No. CSC201806290014). Many thanks to Prof. M. Sadighi for his constructive suggestions which have helped to improve this work. Similar thanks to Dr. M. R. Talagani for help with the validation and verification of the FE model.

## References

[1] C.S. Tang, J.D. Zimmerman, J.I. Nelson, Managing new product development and supply chain risks: The Boeing 787 case, Supply Chain Forum: An International Journal 10 (2) (2009) 74–86.
[2] J. Bachmann, C. Hidalgo, S. Bricout, Environmental analysis of innovative sustainable composites with potential use in aviation sector—A life cycle assessment review, Science China Technological Sciences 60 (9) (2017) 1301–1317.
[3] J. Körbelin, M. Derra, B. Fiedler, Influence of temperature and impact energy on low velocity impact damage severity in CFRP, Compos. A Appl. Sci. Manuf. 115 (2018) 76–87.
[4] S. Abrate, Impact on laminated composite materials, (1991).
[5] A. Wagih, P. Maimí, N. Blanco, J. Costa, A quasi-static indentation test to elucidate the sequence of damage events in low velocity impacts on composite laminates, Compos. A Appl. Sci. Manuf. 82 (2016) 180–189.
[6] A. Wagih, P. Maimí, E.V. González, N. Blanco, J.R.S. de Aja, F.M. de la Escalera, R. Olsson, E. Alvarez, Damage sequence in thin-ply composite laminates under out-of-plane loading, Compos. A Appl. Sci. Manuf. 87 (2016) 66–77.
[7] S. Abrate, Impact on laminated composites: recent advances, Appl. Mech. Rev. 47 (11) (1994) 28.
[8] D.J. Bull, S.M. Spearing, I. Sinclair, Investigation of the response to low velocity impact and quasi-static indentation loading of particle-toughened carbon-fibre composite materials, Compos. A Appl. Sci. Manuf. 74 (2015) 38–46.
[9] D.J. Bull, A.E. Scott, S.M. Spearing, I. Sinclair, The influence of toughening-particles in CFRPs on low velocity impact damage resistance performance, Compos. A Appl. Sci. Manuf. 58 (2014) 47–55.
[10] A. Soto, E.V. González, P. Maimí, F. Martín de la Escalera, J.R. Sainz de Aja, E. Alvarez, Low velocity impact and compression after impact simulation of thin ply laminates, Compos. A Appl. Sci. Manuf. 109 (2018) 413–427.
[11] M. Richardson, M. Wisheart, Review of low-velocity impact properties of composite materials, Compos. A Appl. Sci. Manuf. 27 (12) (1996) 1123–1131.
[12] D. Quan, U. Farooq, G. Zhao, C. Dransfeld, R. Alderliesten, Recycled carbon fibre mats for interlayer toughening of carbon fibre/epoxy composites, Mater. Des. 218 (2022) 110671.
[13] G. Xu, H. Cheng, K. Zhang, B. Liang, Y. Cheng, J. Hu, C. Liu, Modeling of damage behavior of carbon fiber reinforced plastic composites interference bolting with sleeve, Mater. Des. 194 (2020) 108904.
[14] Z. Sun, C. Li, Y. Tie, Experimental and numerical investigations on damage accumulation and energy dissipation of patch-repaired CFRP laminates under repeated impacts, Mater. Des. 202 (2021) 109540.
[15] J. Jiang, Z. Zhang, J. Fu, K.R. Ramakrishnan, C. Wang, H. Wang, Impact damage behavior of lightweight CFRP protection suspender on railway vehicles, Mater. Des. 213 (2022) 110332.
[16] G. Allegri, Modelling fatigue delamination growth in fibre-reinforced composites: Power-law equations or artificial neural networks?, Mater Des. 155 (2018) 59–70.
[17] W. Cui, M. Wisnom, M. Jones, A comparison of failure criteria to predict delamination of unidirectional glass/epoxy specimens waisted through the thickness, Composites 23 (3) (1992) 158–166.
[18] A.C. Orifici, I. Herszberg, R.S. Thomson, Review of methodologies for composite material modelling incorporating failure, Compos. Struct. 86 (1–3) (2008) 194–210.
[19] G. Davies, P. Robinson, J. Robson, D. Eady, Shear driven delamination propagation in two dimensions, Compos. A Appl. Sci. Manuf. 28 (8) (1997) 757–765.
[20] W. Cui, M. Wisnom, A combined stress-based and fracture-mechanics-based model for predicting delamination in composites, Composites 24 (6) (1993) 467–474.
[21] G. Bostaph, W. Elber, A fracture mechanics analysis for delamination growth during impact on composite plates, 1983.
[22] M. Wisnom, Interface element approach to modelling mode I and II fracture, International Conference on Composite Materials, Whistler, Canada, August, 1995, pp. 77-83.
[23] M. De Moura, J. Gonçalves, Modelling the interaction between matrix cracking and delamination in carbon–epoxy laminates under low velocity impact, Composites Science Technology 64 (7–8) (2004) 1021–1027.
[24] H. Hahn, A mixed-mode fracture criterion for composite materials, J. Compos. Tech. Res. 5 (1) (1983) 26–29.
[25] H. Hahn, T. Johannesson, A correlation between fracture energy and fracture morphology in mixed-mode fracture of composites, Elsevier, Mechanical Behaviour of Materials, 1984, pp. 431–438.
[26] J.D. Whitcomb, Analysis of instability-related growth of a through-width delamination, National Aeronautics and Space Administration, Langley Research Center, 1984.
[27] S. Donaldson, Fracture toughness testing of graphite/epoxy and graphite/PEEK composites, Composites 16 (2) (1985) 103–112.
[28] R.A. Jurf, R.B. Pipes, Interlaminar fracture of composite materials, J. Compos. Mater. 16 (5) (1982) 386–394.
[29] S.R. White, Mixed-mode interlaminar fracture of graphite/epoxy composites, Washington University, 1987.
[30] S. Hashemi, A. Kinloch, J. Williams, The effects of geometry, rate and temperature on the mode I, mode II and mixed-mode I/II interlaminar fracture of carbon-fibre/poly (ether-ether ketone) composites, J. Compos. Mater. 24 (9) (1990) 918–956.
[31] X.Q. Van, S.Y. Du, W. Duo, An engineering method of determining the delamination fracture toughness of composite laminates, Eng. Fract. Mech. 39 (4) (1991) 623–627.
[32] S. Hashemi, A.J. Kinloch, G. Williams, Mixed-mode fracture in fiber-polymer composite laminates, Composite materials: Fatigue fracture. 3 (1991) 143–168.
[33] M.L. Benzeggagh, M. Kenane, Measurement of mixed-mode delamination fracture toughness of unidirectional glass/epoxy composites with mixed-mode bending apparatus, Composites Science Technolog 56 (4) (1996) 439–449.
[34] K.I. Tserpes, P. Papanikos, T. Kermanidis, A three-dimensional progressive damage model for bolted joints in composite laminates subjected to tensile loading, Fatigue Fract. Eng. Mater. Struct. 24 (10) (2001) 663–675.
[35] J.D. Lee, Three dimensional finite element analysis of damage accumulation in composite laminate, Comput. Struct. 15 (3) (1982) 335–350.
[36] O.O. Ochoa, J.J. Engblom, Analysis of progressive failure in composites, Compos. Sci. Technol. 28 (2) (1987) 87–102.
[37] R. Long, Static strength of adhesively bonded ARALL-1 joints, J. Compos. Mater. 25 (4) (1991) 391–415.
[38] R. Luo, E. Green, C. Morrison, Impact damage analysis of composite plates, Int. J. Impact Eng. 22 (4) (1999) 435–447.
[39] X. Zhang, Impact damage in composite aircraft structures-experimental testing and numerical simulation, Proceedings of the Institution of Mechanical Engineers, Part G: Journal of Aerospace Engineering 212 (4) (1998) 245–259.
[40] M. De Moura, A. Marques, Prediction of low velocity impact damage in carbon–epoxy laminates, Compos. A Appl. Sci. Manuf. 33 (3) (2002) 361–368.
[41] X. Li, D. Ma, H. Liu, W. Tan, X. Gong, C. Zhang, Y. Li, Assessment of failure criteria and damage evolution methods for composite laminates under low-velocity impact, Compos. Struct. 207 (2019) 727–739.
[42] K. Kodagali, Progressive Failure Analysis of composite Materials using the, Puck Failure Criteria (2017).
[43] C.-S. Lee, J.-H. Kim, S.-K. Kim, D.-M. Ryu, J.-M. Lee, Initial and progressive failure analyses for composite laminates using Puck failure criterion and damage-coupled finite element method, Compos. Struct. 121 (2015) 406–419.
[44] R. Rodi, R. Alderliesten, R. Benedictus, Crack-tip behavior in fiber/metal laminates by means of digital-image correlation, Journal of Aircraft 47 (5) (2010) 1636–1646.
[45] N. Sela, O. Ishai, Interlaminar fracture toughness and toughening of laminated composite materials: a review, Composites 20 (5) (1989) 423–435.
[46] ASTM, Standard Test Method for Measuring the Damage Resistance of a Fiber-Reinforced Polymer Matrix Composite to a Drop-Weight Impact Event, ASTM International 100 Barr Harbor Drive, PO Box C700, West Conshohocken, PA 19428-2959, United States (2017).
[47] ASTM, Standard Test Method for Measuring the Damage Resistance of a Fiber-Reinforced Polymer Matrix Composite to a Drop-Weight Impact Event, ASTM International 100 Barr Harbor Drive, PO Box C700, West Conshohocken, PA 19428-2959, United States (2020).
[48] G.A. Davies, X. Zhang, Impact damage prediction in carbon composite structures, Int. J. Impact Eng. 16 (1) (1995) 149–170.
[49] J.P. Hou, N. Petrinic, C. Ruiz, S. Hallett, Prediction of impact damage in composite plates, Compos. Sci. Technol. 60 (2) (2000) 273–281.
[50] F. Esrail, C. Kassapoglou, An efficient approach for damage quantification in quasi-isotropic composite laminates under low speed impact, Compos. B Eng. 61 (2014) 116–126.
[51] R. Pippan, A. Hohenwarter, Fatigue crack closure: a review of the physical phenomena, Fatigue Fract. Eng. Mater. Struct. 40 (4) (2017) 471–495.
[52] R. Pippan, W. Grosinger, Fatigue crack closure: From LCF to small scale yielding, Int. J. Fatigue 46 (2013) 41–48.
[53] N. van Hoorn, C. Kassapoglou, S. Turteltaub, W. van den Brink, Experimental damage tolerance evaluation of thick fabric carbon/epoxy laminates under low-velocity and high-velocity impact and compression-after-impact, J. Compos. Mater. 00219983211060501 (2022).
[54] K. Huang, A. de Boer, R. Akkerman, Analytical modeling of impact resistance and damage tolerance of laminated composite plates, AIAA journal 46 (11) (2008) 2760–2772.
[55] C.R. Steele, C.D. Balch, Introduction to the Theory of Plates, Department of Mechanical Engineering Stanford University, Division of Mechanics and Computation, 2009.
[56] D. Hull, Y.B. Shi, Damage mechanism characterization in composite damage tolerance investigations, Compos. Struct. 23 (2) (1993) 99–120.
[57] K.D. Challenger, The damage tolerance of carbon fiber reinforced composites—A workshop summary, Compos. Struct. 6 (4) (1986) 295–318.
[58] J.C. Prichard, P. Hogg, The role of impact damage in post-impact compression testing, Composites 21 (6) (1990) 503–511.
[59] G. Davies, R. Olsson, Impact on composite structures, The Aeronautical Journal 108 (1089) (2004) 541–563.

[60] D. Liu, Impact-induced delamination—a view of bending stiffness mismatching, J. Compos. Mater. 22 (7) (1988) 674–692.
[61] S. Freeman, Characterization of lamina and interlaminar damage in graphite/epoxy composites by the deply technique, ASTM, International (1982).
[62] M. Shokrieh, L. Lessard, C. Poon, Three-dimensional progressive failure analysis of pin/bolt loaded composite laminates, AGARD Conference Proceedings (1996).